CO_2 Reduction Hot Paper

How to cite: *Angew. Chem. Int. Ed.* **2022**, *61*, e202114648
International Edition: doi.org/10.1002/anie.202114648
German Edition: doi.org/10.1002/ange.202114648

Imparting CO_2 Electroreduction Auxiliary for Integrated Morphology Tuning and Performance Boosting in a Porphyrin-based Covalent Organic Framework

Yi-Rong Wang, Hui-Min Ding, Xiao-Yu Ma, Ming Liu, Yi-Lu Yang, Yifa Chen, Shun-Li Li, and Ya-Qian Lan**

Abstract: *Strategies that enable simultaneous morphology-tuning and electroreduction performance boosting are much desired for the exploration of covalent organic frameworks in efficient CO_2 electroreduction. Herein, a kind of functionalizing exfoliation agent has been selected to simultaneously modify and exfoliate bulk COFs into functional nanosheets and investigate their CO_2 electroreduction performance. The obtained nanosheets (Cu–Tph–COF–Dct) with large-scale ($\approx$1.0 μm) and ultrathin ($\approx$3.8 nm) morphology enable a superior FE_{CH4} ($\approx$80 %) (almost doubly enhanced than bare COF) with large current-density ($-220.0\ mA\ cm^{-2}$) at −0.9 V. The boosted performance can be ascribed to the immobilized functionalizing exfoliation agent (Dct groups) with integrated amino and triazine groups that strengthen CO_2 absorption/activation, stabilize intermediates and enrich the CO concentration around the Cu active sites as revealed by DFT calculations. The point-to-point functionalization strategy for modularly assembling Dct-functionalized COF catalyst for CO_2 electroreduction will open up the attractive possibility of developing COFs as efficient CO_2RR electrocatalysts.*

Introduction

The efficient electrochemical conversion of greenhouse gas (i.e. CO_2) is of vital significance for alleviating environmental crisis and climate change.[1] Among them, CO_2 electrochemical reduction reaction (CO_2RR) enables the transformation of CO_2 into serviceable high-valued chemicals or fuels (e.g., CH_4, C_2H_4, C_2H_5OH and HCOOH, etc.) by renewable electricity, which would simultaneously mitigate the energy crisis caused by the shortage of fossil fuels.[2] For the CO_2 reduction products, hydrocarbon fuels (e.g., CH_4 or C_2H_4) with high selectivity are regarded as the ideal reduction products due to their large demand as important precursors for various chemicals or plastics in market domain.[3] Nevertheless, CO_2RR is thermodynamically and kinetically sluggish owing to the chemical inertness of CO_2 with a low standard molar Gibbs free energy of formation ($-394.4\ kJ\ mol^{-1}$) as well as the high dissociation energy ($803\ kJ\ mol^{-1}$) of C=O bond, leading to the low selectivity and efficiency.[4] In addition, the conversion of CO_2 to hydrocarbon fuels are still restricted by the competing thermodynamically favorable hydrogen evolution reaction (HER) and multiple proton-coupled electron transfer processes during the CO_2RR process, in which different conversion pathways would occur under similar reduction potentials and result in relatively low selectivity.[5] Therefore, the development of new-concept electrocatalysts would be the most challenging step to concurrently achieve high activity and selectivity for specific hydrocarbon products.

Up to date, Cu-based catalysts, including Cu nanomaterials,[6] Cu cyclams[7] and Cu oxides[8] have been proved to have unique advantages in CO_2RR to hydrocarbons or alcohols with appreciable activity and selectivity owing to their negative adsorption energy for CO* and positive adsorption energy for H* compared with other transition-metal systems.[9] However, the high CO_2RR selectivity towards specific hydrocarbons, such as CH_4, C_2H_4 or C_3H_8, still remains a daunting challenge due to the lack of specific Cu-based electrocatalysts. In the generally reported CO_2RR process, CO_2 is firstly converted to adsorbed CO adsorbate (*CO) followed by its further reduction to hydrocarbons and oxygenates on Cu surfaces, acting like a domino process.[10] The formation of *CO and hydrocarbons requires the optimal binding strength for *COOH and *CO, respectively. Simultaneous optimizing of these processes on a single reactive site is challenging due to the linear scaling relationship of the binding strength of key intermediates (e.g., *COOH and *CO) as well as kinetic linear scaling relation between intermediate adsorption and activation energy, resulting in low selectivity of hydrocarbon products.[11] To this end, the key steps are mostly limited by the lack of desired platform that can break these two linear scaling relations. By increasing the flux of CO on the Cu-based catalyst surface, adsorbed CO can migrate to Cu sites and further reduction to methane, which will also suppress the competitive HER by weakening the binding strength of H_{ads}.[12] Hence, the combination of Cu site and CO-producing site might be a promising strategy to

[*] Dr. Y.-R. Wang, H.-M. Ding, X.-Y. Ma, M. Liu, Y.-L. Yang, Prof. Y. Chen, S.-L. Li, Prof. Y.-Q. Lan
Jiangsu Collaborative Innovation Centre of Biomedical Functional Materials, Jiangsu Key Laboratory of New Power Batteries, School of Chemistry and Materials Science, Nanjing Normal University
Nanjing 210023 (P. R. China)
E-mail: chyf927821@163.com
yqlan@njnu.edu.cn
Homepage: https://www.yqlangroup.com
Prof. Y.-Q. Lan
School of Chemistry, South China Normal University
Guangzhou, 510006 (P. R. China)
E-mail: yqlan@m.scnu.edu.cn
Supporting information and the ORCID identification number(s) for the author(s) of this article can be found under: https://doi.org/10.1002/anie.202114648.

improve the selectivity of hydrocarbon products like CH_4 by increasing the CO concentration.[11a,b,13] During past decades, pioneering strategies like Cu-Zn,[14] Cu-Au,[15] and Cu-Ag[11a] based bimetallic tandem catalysts have been developed, in which one of the component serves as the CO-producing site to increase the concentration of CO around Cu to achieve the production of hydrocarbons. Despite the progress achieved, the investigation in this area is still at the early stage and there are still some unresolved problems, such as: 1) the low utilization efficiency of CO intermediate species at the Cu sites due to their random or uncontrollable diffusion between CO-producing and Cu sites; 2) the low CO_2 adsorption/activation ability due to the lack of powerful interaction sites or high porosity; 3) the stabilization, transmission and utilization of CO intermediate species are challenging due to the lack of directional channels or accessible distance between CO-producing and Cu active sites; 4) most of the reported materials are not crystalline ones, which generally lack in well-defined crystalline models to understand the specific structure-performance relationship and conversion mechanism for CO_2RR.

Covalent organic frameworks (COFs), a class of porous crystalline frameworks that are connected and extended periodically through strong covalent bonds, have been applied in proton conduction, catalysis, gas storage/separation and sensing, etc.[16] COFs possess unique features like tunable structure, high crystallinity, accessible pore channels and large surface areas are regarded as ideal platforms for mass transport, CO_2 adsorption, diffusion, and activation during the CO_2RR process.[17] Especially attractive are their advantages in the structure design and function tuning, which can endow COFs with multi-functionality for much preferred multi-catalytic sites for the generation of various CO_2 reduction products like hydrocarbons. Besides, the emerging reticular chemistry has demonstrated the possibility of modularly point-to-point assembly of active centers at the atomic/molecular levels, thereby lending credence to introduce a CO-producing site around the Cu active site to achieve uniform molecular modification of all metal sites in the assembled COFs. Moreover, the abundant channels of COFs will be beneficial for the stabilization, transmission and utilization of CO intermediate species during CO_2RR. In addition, it is notable that the exfoliation of COFs can expose more accessible active sites and larger surface area for being beneficial to increase the contact with reactant and intermediate molecules.[18] Thus, the introduction of typical CO_2RR centers with CO-producing sites in COFs nanosheets to explore the intrinsic multi-catalytic sites and specific reaction pathways in producing hydrocarbons like CH_4 would be quite interesting and crucial.

Herein, we have reported a strategy based on functionalizing exfoliation agent to simultaneously modify and exfoliate COF into large-scale ($\approx$1.0 μm) and ultrathin ($\approx$3.8 nm) nanosheets (Cu–Tph–COF–Dct). The functionalizing exfoliation agent (2,4-diamino-6-cholo-1,3,5-triazine, denoted as Dct) can serve as the CO_2 reduction auxiliary for domino morphology tuning and performance boosting in CO_2RR catalyst, in which the immobilized Dct with triazine and amino groups can strengthen the absorption/activation of CO_2, stabilize the active intermediates and facilitate the generation of CO to enrich the CO concentration around the Cu active sites. Specifically, the optimized COF system, which comprises sequential Cu-porphyrin and Dct catalysis units, achieves FE of $\approx$80 % and current density of -220.0 mA cm^{-2} for CH_4 at -0.90 V, which is almost doubly enhanced when compared with bare COF and superior to most of Cu-based electrocatalysts. Moreover, the vital role of Dct as CO_2 reduction auxiliary and the detailed catalytic mechanism are systematically studied by the DFT calculations. This work not only presents a molecular functionalization and exfoliation concept of COF based electrocatalysts but also offers intuitive understandings of hydrocarbon generation and catalyst optimization for electrocatalytic CO_2RR and beyond.

Results and Discussion

The Cu–Tph–COF–OH was synthesized via a solvothermal method based on the previous reported literature.[19] Then, Cu–Tph–COF–Dct was prepared by the reaction of Cu–Tph–COF–OH and functionalizing exfoliation agent (2,4-diamino-6-cholo-1,3,5-triazine (Dct)) at 90 °C in a mixed solvent of 1,4-dioxane and triethylamine (detail see Methods) (Figure 1 a). For Cu–Tph–COF–OH, the covalent connecting between 2,5-dihydroxy-p-benzaldehyde (Dha) and tetrakis(4-aminophenyl)-porphinato (TAPP) generates the one-dimensional channel (pore size, 2 nm) and the theoretically distance between the COF-stacking layers is $\approx$4 Å (Figure S1).[19] The -OH groups in Cu–Tph–COF–OH can be modified with other functional units like Dct to generate powerful catalysis system. After modification, the PXRD pattern shows that the

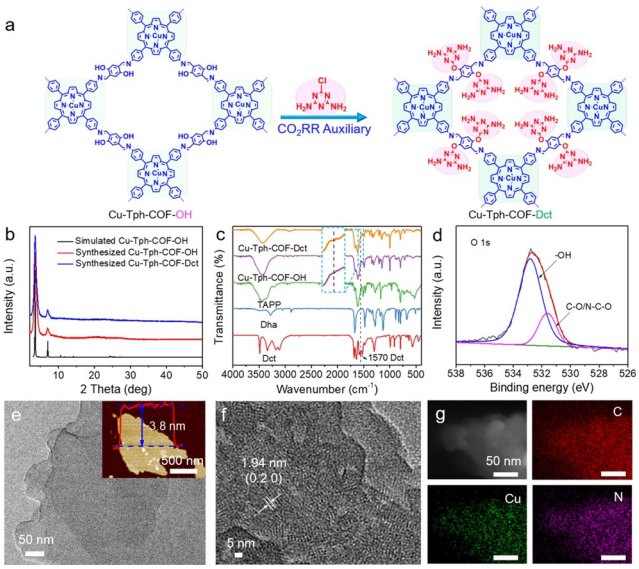

Figure 1. The preparation and characterization of Cu–Tph–COF–OH and Cu–Tph–COF–Dct. a) The Scheme of the preparation of Cu–Tph–COF–Dct. b) The PXRD patterns of Cu–Tph–COF–OH and Cu–Tph–COF–Dct. c) The FT-IR spectra. d) The XPS spectroscopy of Cu–Tph–COF–Dct. e) The TEM and AFM (insert) image of Cu–Tph–COF–Dct. f) The HRTEM image of Cu–Tph–COF–Dct. g) STEM and mapping images of Cu–Tph–COF–Dct.

synthesized Cu–Tph–COF–Dct is in good agreement with that of Cu–Tph–COF–OH, confirming the well-remained crystallinity after modification treatment (Figure 1b). In addition, the FT-IR spectra and XPS have been performed to prove the covalent-bond modification in Cu–Tph–COF–Dct (Figure 1c and 1d). In the FT-IR spectrum of Cu–Tph–COF–Dct, a new peak appeared at 1570 cm^{-1} is assigned to the triazine ring when compared with that of Cu–Tph–COF–OH, suggesting that the existence of Dct in the Cu–Tph–COF–Dct (Figure 1c).[20] Besides, the disappearance of N-H stretching vibration at 3315 cm^{-1} and a new absorption peak appeared at 999 cm^{-1} when compared with that of TAPP indicate that the metal coordination occurred at the porphyrin center. After modification, the C=N stretching vibration band at 1620 cm^{-1} is still remained in the Cu–Tph–COF–Dct, proving the high stability of COF during the modification process. The X-ray photoelectron spectroscopy (XPS) results show the existence of N–C–O bonds in Cu–Tph–COF–Dct when compared with that of Cu–Tph–COF–OH (Figure 1d and S2). The observed Cu $2p_{3/2}$ binding energy of 934.8 eV and $2p_{1/2}$ binding energy of 954.5 eV are ascribed to Cu^{II} (Figure S3).[21] All these evidences illustrate that Dct group is successfully modified into Cu–Tph–COF–OH through C–O covalent bonds.

The structural porosity and specific surface area are determined using nitrogen adsorption isotherms at 77 K. N_2 adsorption-desorption curves exhibit a typical reversible isotherm, revealing the presence of micropores for Cu–Tph–COF–Dct and Cu–Tph–COF–OH (Figure S4). The BET surface area of Cu–Tph–COF–Dct is calculated to be 335 $cm^2 g^{-1}$ with a total pore volume of 0.23 $cm^3 g^{-1}$, which is smaller than that of pure Cu–Tph–COF–OH (456 $cm^2 g^{-1}$, 0.31 $cm^3 g^{-1}$). The difference is due to the presence of Dct. In addition, quenched solid-state density functional theory (QSDFT) calculation reveals that Cu–Tph–COF–Dct possesses relatively narrow pore size distributions (1.2 to 1.8 nm), in which the intensity of micropore range is lower than Cu–Tph–COF–OH, implying the channel is partially occupied after the modification of Dct groups (Figure S4). In addition, CO_2 adsorption experiments have been performed to examine the CO_2 capability of the as-synthesized Cu–Tph–COF–Dct and Cu–Tph–COF–OH. Cu–Tph–COF–Dct presents CO_2 uptake capacity of 61.4 $cm^3 g^{-1}$ and 32.9 $cm^3 g^{-1}$ at 273 K and 298 K, respectively, which is higher than that of Cu–Tph–COF–OH (47.4 $cm^3 g^{-1}$, 273 K and 29.2 $cm^3 g^{-1}$, 298 K) (Figure S5). Besides, the adsorption enthalpy of Cu–Tph–COF–Dct (25.9 kJ mol^{-1}) is also larger than that of Cu–Tph–COF–OH (20.8 kJ mol^{-1}), implying the introduction of Dct groups can largely enhance the interaction with CO_2. Furthermore, Cu–Tph–COF–Dct also exhibits high chemical stability. After soaking in 1 M KOH solution for more than 12 h, the sample can remain the crystalline structure as proved by the PXRD tests, guaranteeing the further investigation of electrochemical CO_2RR (Figure S6).

The morphology of the as-synthesized Cu–Tph–COF–Dct is investigated by TEM tests (Figure 1e). As shown in Figure S7, the TEM image of Cu–Tph–COF–OH displays bulk cubic morphology. After modification with Dct groups, Cu–Tph–COF–Dct shows a kind of nanosheet morphology, implying the simultaneous exfoliation effect during the modification process (Figure 1e). To estimate the thickness of the obtained Cu–Tph–COF–Dct, AFM test has been performed (insert image in Figure 1e). Interestingly, the results show that the thickness of Cu–Tph–COF–Dct is only $\approx$3.8 nm over a large scale ($\approx$1.0 μm). In the HR-TEM image of Cu–Tph–COF–Dct, the oriented lattice fringes can be observed and the lattice spacing of 1.94 nm is attributed to the (0 2 0) crystal facet of Cu–Tph–COF–OH, confirming the high crystallinity of the obtained Cu–Tph–COF–Dct (Figure 1f). Moreover, the HAADF image and EDX elemental mapping confirm that Cu, C, and N are evenly distributed in Cu–Tph–COF–Dct, suggesting the high elemental homogeneity in the nanosheet (Figure 1g and Figure S8). The specific content of Cu in Cu–Tph–COF–Dct is calculated to be $\approx$5.1 wt% as determined by the ICP-AES test (Table S1), which matches well with the result in EDS test (Figure S8). The above results show that Cu–Tph–COF–Dct with advantages like ultrathin nanosheet morphology, uniformly distributed Cu active sites, high porosity and stability might be much beneficial for its application as efficient electrocatalyst in electrochemical CO_2RR.

To evaluate the electrochemical CO_2RR performance of the as-synthesized Cu–Tph–COF–Dct, all electrochemical tests are performed in flow cell at selected potentials using Pt foil and Ag/AgCl electrode as the counter and reference electrode, respectively. The cathode and anode are separated by an anion exchange membrane. The working electrode is catalyst coated gas diffusion layer (GDL) modified carbon paper. Throughout all the experiments, 1 M KOH electrolyte is flowed in the cathode and anode chambers separately at 7 mL min^{-1} with a peristaltic pump, while CO_2 gas is flowed pass through the GDL at a rate of 20 sccm with a mass flow controller. The CO_2 mass transfer along the triple-phase boundary is greatly enhanced with GDL, thus achieving substantially large current density.[11a,22] The detailed Scheme of the flow cell test setup is presented in Figure S9. In this work, all potentials are measured using Ag/AgCl electrode and the results are reported relative to the RHE.

For the initial performance comparison, LSV curves are firstly recorded to assess the electrocatalysis activity under the applied potential varying from 0 to −1.1 V vs. RHE. According to the LSV polarization curves, Cu–Tph–COF–Dct shows a total current density of −537.4 mA cm^{-2} at −1.1 V, which is superior to Cu–Tph–COF–OH (−394.2 mA cm^{-2}), indicating the high activity towards electrocatalysis (Figure 2a). In flowing CO_2 atmosphere, Cu–Tph–COF–Dct shows a lower onset potential and larger current density than that in Ar, indicating the high electrochemical performance of Cu–Tph–COF–Dct indeed derive from CO_2RR (Figure S12a). In order to further assess the selectivity of catalysts during the CO_2RR, the electrolysis experiments are carried out at selected potentials varying from −0.7 to −1.0 V vs. RHE. The gas reduction products from CO_2RR are detected and analyzed by online GC (Figure S10-12). As a result, CH_4, C_2H_4, CO, and H_2 are found to be the gas reduction products from electrocatalysis (Figure 2b). The FE of products at different applied potentials are calculated and the sum of FE is found to be $\approx$100%

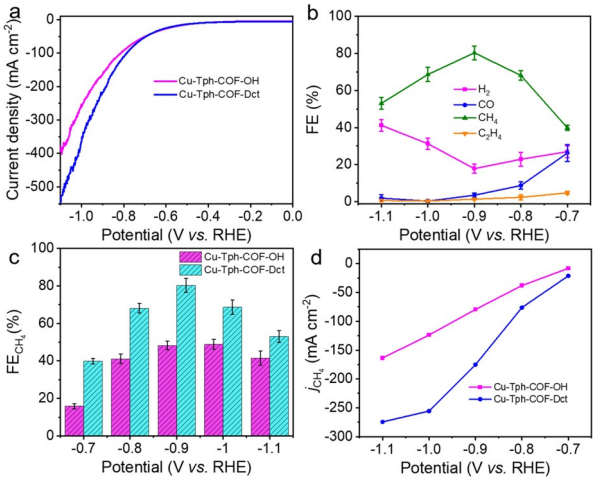

Figure 2. CO_2RR performance of Cu–Tph–COF–OH and Cu–Tph–COF–Dct. a) Linear sweep voltammetric curves. b) Faradaic efficiencies of CO_2RR products at different applied potentials for Cu–Tph–COF–Dct. All reported values are average ones calculated from three or more independent measurements, and all errors are given as standard deviations. c) Faradaic efficiencies for CH_4 at different applied potentials of Cu–Tph–COF–OH and Cu–Tph–COF–Dct. d) Partial CH_4 current density.

at all potentials. For Cu–Tph–COF–Dct, it gives the highest FE_{CO} ($26.3 \pm 4.4\,\%$) at -0.7 V with a current density of $-53.2\ mA\,cm^{-2}$ along with $27.0 \pm 3.2\,\%$ FE_{H2}, $39.8 \pm 1.4\,\%$ CH_4 and negligible C_2H_4 ($4.8 \pm 0.7\,\%$) (Figure 2b and S13). The ^{1}H nuclear magnetic resonance spectroscopy indicates that there are negligible liquid products obtained from the electrocatalysis under the optimal test conditions (Figure S14). With the increase of potential, the FE_{CO} continuously decreases. The FE_{CH4} is increased over the applied potential ranging from -0.7 to -0.9 V and reaches up to the maximum value of $\approx 80\,\%$ at -0.9 V and keeps higher than 68 % over a wide potential range from -0.8 to -1.0 V in KOH solution (Figure 2b), which is one of the best CO_2RR-to-CH_4 performances to date.[4c,10a,22b,23] The total FE of CO_2RR is larger than HER over the entire applied potential range from -0.7 to -1.1 V and the highest FE_{CO2RR} is $85.2 \pm 2.5\,\%$ at -0.9 V and keeps higher than 70 % from -0.7 to -1.0 V (Figure S15), implying the higher selectivity of Cu–Tph–COF–Dct catalyst towards CO_2RR than that of HER. Cu–Tph–COF–Dct with the properties of large active current density and high CH_4 selectivity at a low reductive potential is superior to most of the reported Cu-based CO_2RR systems under alkaline condition tested in both flow cell and H-type cell setups (Table S2).[4c,10a,22b,23] Moreover, Cu–Tph–COF–Dct with diverse Dct amounts are synthesized and utilized for CO_2RR test (denoted as Cu–Tph–COF–Dct–x ($x = 1, 2, 3$); Cu–Tph–COF–Dct-1 represent for Cu–Tph–COF–Dct). As shown in Figure S16, the as-synthesized samples present similar PXRD patterns to the simulated ones, indicating the remained crystallinity. The result show that Cu–Tph–COF–Dct-2 and Cu–Tph–COF–Dct-3 can reach up to the highest $FE_{CH4} = 57.9 \pm 2.9\,\%$ and $68.7 \pm 3.9\,\%$ at -1.0 V and -0.9 V, respectively, implying the Cu–Tph–COF–Dct-1 to be the optimal Dct modification sample (Figure S17 and S18). Meanwhile, the Dct has no CO_2 reduction performance (Figure S19). Besides, Cu–Tph–COF–OH gives a large FE_{H2} ($53.6 \pm 2.8\,\%$) at -0.7 V with a current density of $-51\ mA\,cm^{-2}$ and the highest FE_{CH4} is only $48.8 \pm 2.6\,\%$ at -1.0 V (Figure 2c and S20). In addition, Tph-COF-OH (no Cu in porphyrin center) has no CO_2 reduction performance (Figure S21). The superior performance of Cu–Tph–COF–Dct indicates the synergistic effect of Dct groups and Cu centers in electrochemical CO_2RR.

To investigate the catalytic activity of CO_2RR performance for Cu–Tph–COF–Dct, the partial current densities of CH_4, CO, C_2H_4 and H_2 at various potentials are calculated (Figure 2d and Figure S13). Cu–Tph–COF–Dct displays a high partial CH_4 current density of $-175.2\ mA\,cm^{-2}$ at -0.9 V, which is doubly enhanced than that of Cu–Tph–COF–OH ($-79.5\ mA\,cm^{-2}$) (Figure 2d). To further reveal the activity of Cu–Tph–COF–Dct for CO_2RR, chronoamperometric curves at different applied potentials on Cu–Tph–COF–Dct are performed (Figure S22). All the current density gained at potentials varying from -0.7 V to -1.0 V shows a negligible decay, implying that the catalytic activity of Cu–Tph–COF–Dct can remain stable. Remarkably, it can reach up to high current density of about -220 and $-372\ mA\,cm^{-2}$ at -0.9 and -1.0 V, respectively. Besides, the bare carbon paper is measured and no electrocatalytic CO_2RR activity is detected (Figure S23). Moreover, the PVDF is used as binder to fabricate the working electrode to explore its CO_2RR performance (Figure S24). The result show that the Cu–Tph–COF–Dct can reach up to the highest $FE_{CH4} = 79.6 \pm 5.3\,\%$ at -0.9 V. The remained high FE_{CH4} indicate the binder has no apparent effect on the generation of electrocatalytic products. In addition, to verify the carbon source of the reduction gas products, the isotopic-labeling experiment that using $^{13}CO_2$ as substrate is conducted under identical reaction condition and the products are analyzed by GC-MS. As displayed in Figure 3a and Figure S25, the peaks at $m/z = 17$, 29 and 30 are attributed to $^{13}CH_4$, ^{13}CO and $^{13}C_2H_4$, respectively, suggesting that the carbon sources of reduction gas products come from the CO_2 conversion.

Additionally, the enhanced CO_2RR performance of Cu–Tph–COF–Dct might contribute to the electrochemically active surface area (ECSA). To discuss the potential influence factors of Cu–Tph–COF–Dct with remarkable performance, the electrochemical double-layer capacitance (C_{dl}) is calculated to evaluate the ECSA (Figure S26). The results demonstrate that Cu–Tph–COF–Dct presents larger C_{dl} value ($5.83\ mF\,cm^{-2}$) than that of Cu–Tph–COF–OH ($4.32\ mF\,cm^{-2}$). It indicates that Cu–Tph–COF–Dct contains larger accessible catalytic area and more effective active sites to contact with the electrolyte for electrocatalysis, leading to enhanced CO_2RR performance. Furthermore, to reveal the electrocatalytic kinetics on the electrode/electrolyte surface of Cu–Tph–COF–OH and Cu–Tph–COF–Dct during electrochemical CO_2RR, the EIS tests of samples are recorded under the potential of -0.9 V vs. RHE (Figure S27). As shown in the Nyquist plots, Cu–Tph–COF–Dct exhibits smaller charge transfer resistance (22.23 Ω) than that of Cu–Tph–COF–OH (26.47 Ω), implying Cu–Tph–COF–Dct enables to provide faster electron transfer from the catalyst

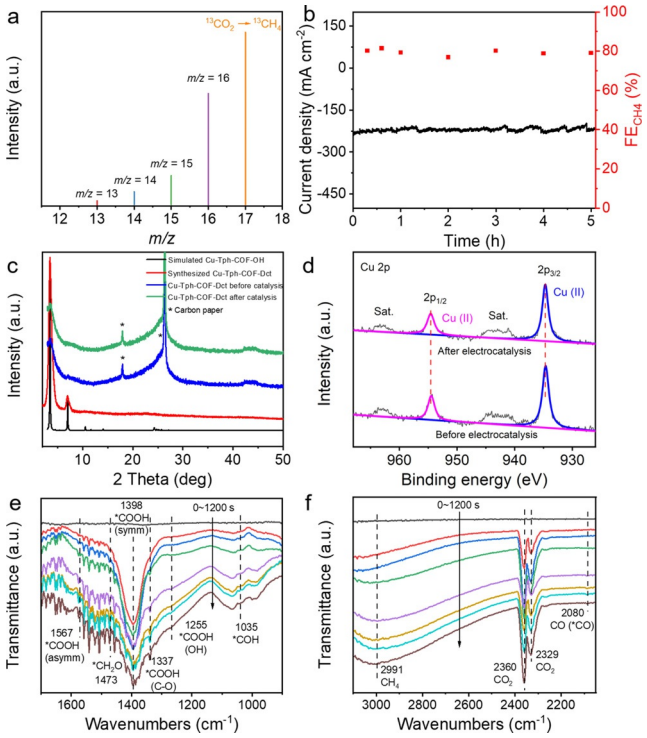

Figure 3. CO_2RR performance of Cu–Tph–COF–OH and Cu–Tph–COF–Dct. a) The mass spectra of $^{13}CH_4$ recorded under $^{13}CO_2$ atmosphere. b) Durability test of Cu–Tph–COF–Dct at the potential of −0.9 V vs. RHE. c) The PXRD patterns of Cu–Tph–COF–Dct modified GDL-carbon paper electrodes before and after tests. d) The XPS spectroscopy of Cu–Tph–COF–Dct before and after CO_2RR tests. e, f) In-situ ATR-FTIR spectra of Cu–Tph–COF–Dct during the electrochemical CO_2RR.

surface to the reactant in intermediate generation, eventually resulting in the enhancement of activity and selectivity.

Stability is a vital parameter to evaluate the durability properties of catalysts for further applications. To access the electrochemical stability of Cu–Tph–COF–Dct, long-term durability test is measured via chronoamperometric curves under the optimal potential of −0.9 V through monitoring variations in FE_{CH4} at intervals (Figure 3b). The current density of Cu–Tph–COF–Dct remains stable centered at approximately −217 mA cm^{-2}. In addition, the FE of CH_4 exhibits slight decay compared with the initial one and keeps at ≈80% for 5 h, implying the Cu–Tph–COF–Dct can maintain both the activity and selectivity during the CO_2 reduction process. In the literature,[24] the Cu-N interaction in the discrete molecular CuPc catalyst seems to be not strong enough to stabilize the copper ion centers, and the aggregation of these atomically dispersed Cu atoms leads to the generation of Cu clusters and nanoparticles. By comparison, some Cu phthalocyanines or cyclams[7] based MOF catalysts can remain the high stability during the CO_2RR process, which indicates that the samples with periodically extended framework structures might endure the CO_2RR process without dementalization. Thus, the structural stability of the Cu–Tph–COF–Dct electrocatalyst before and after electrocatalysis have been characterized and investigated. The PXRD patterns suggest that there is no phase transition or obvious structural change after electrocatalytic tests (Figure 3c). Furthermore, the state of Cu species after electrocatalysis is also revealed by XPS tests (Figure 3d). The Cu 2p spectra of Cu–Tph–COF–Dct electrodes after the test are similar to those of fresh ones and there are no Cu and Cu^I observed, revealing that the Cu species show no obvious change after CO_2RR. These results demonstrate that Cu–Tph–COF–Dct is a kind of stable electrocatalyst, which has much potential to be used in efficient electrochemical CO_2RR (Figure S28 and Table S3).

To ascertain the intermediates during the CO_2RR process, in-situ ATR-FTIR measurements are performed (Figure 3 e and f). The bands at 1255 cm^{-1}, 1337 cm^{-1}, 1398 cm^{-1} and 1567 cm^{-1} in the spectra are assigned to the OH deformation, C-O stretch, symmetric stretch, asymmetric stretch of *COOH intermediate, respectively. These important intermediates are regarded as the key intermediates for the formation of CO or CH_4.[4c,7a,25] The chemisorbed CO (*CO) peak is detected at 2080 cm^{-1}, a blue shift in comparison with that most of the reported value of 2065 cm^{-1}, which may be stabilized by the hydrogen bonding formed between *CO and -NH_2 group of Dct (Figure 3 f).[4c,7a,25] Such a significant amount of surface *CO is believed to trigger the production of multi electron products.[4c,7a,25] Moreover, the signals appeared at 1035 cm^{-1}, 1473 cm^{-1} can be assigned to *COH and *CH_2O, respectively (Figure 3e), which are the crucial intermediates for CO_2RR to CH_4.[4c,7a,25]

To gain more insight into the electrocatalytic mechanism, density functional theory (DFT) calculations related to CO_2 adsorption and activation are conducted to confirm the active sites (Figure 4a and Figure S29). Interestingly, in the first step of CO_2RR, the adsorption of CO_2 molecule on the -NH_2

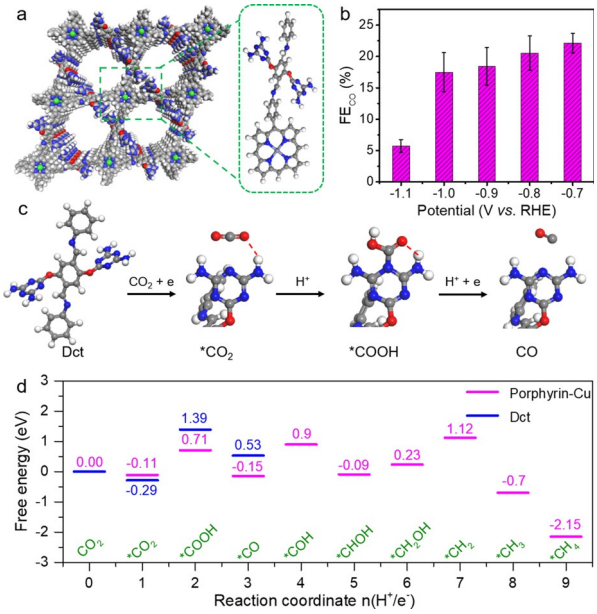

Figure 4. Mechanism and DFT calculations. a) Schematic of DFT calculation units. b) FE for CO recorded at different potentials on Tph-COF-Dct. c) The CO_2-to-CO conversion reactive pathway and intermediate architectures over Dct molecule of Cu–Tph–COF–Dct. d) Free energy profiles for CO_2-to-CO and CO_2-to-CH_4 reaction pathway on Dct and porphyrin-Cu, respectively.

group (Lewis-basic site) of Dct is stronger than that of Cu sites, corresponding to adsorption energies of −0.29 eV and −0.11 eV for the formation of $*CO_2$, respectively (Figure 4c and Figure 4d). In the following processes on the Dct fragment, the CO_2 transfers to the neighboring triazine N atom to form the *COOH and *CO, thus promoting the formation of CO (Figure 4c and Figure 4d). This result is consistent with the obtained results of Tph-COF-Dct (no Cu in porphyrin center compared to Cu−Tph−COF−Dct), in which its FE_{CO} can reach to 22% at −0.7 V (Figure 4b). The calculation and experiment results indicate that the CO_2RR can readily occur at the triazine center of Dct with the assistance of amino group, during which the Dct groups would possess hydrogen-bonding interaction with the activated CO_2 intermediate to increase CO_2 adsorption and stabilize intermediate, thus increasing the concentration of CO to largely enhance the activity and selectivity.

After revealing the active sites in Dct, DFT calculations are subsequently conducted to reveal the detailed free energy profiles for each reaction coordinate during CO_2-to-CH_4 pathways on Cu−Tph−COF−Dct. Interestingly, as revealed in the DFT calculations results, the Cu sites can be reduced by the formation of *H on the surrounding N sites under electroreduction conditions as shown in Figure S30, which sets basis for the deep reduction of CO_2. In general, the formation of CH_4 has two possible reaction pathways including *HCOOH pathway or *CO pathway as supported by the reported literature.[11,14,15] As mentioned above, the main CO_2 reduction products of Cu−Tph−COF−Dct are CH_4 and CO, and the CO production decreases following the formation of CH_4. It could be deduced that the *CO pathway is occurred on Cu−Tph−COF−Dct, including $*CO_2$, *COOH, *CO, *COH, *CHOH, $*CH_2OH$, $*CH_2$, $*CH_3$ and $*CH_4$, coupling with the following multi-step proton-electron transfer processes. The free energy pathway of CO_2-to-CH_4 conversion on Cu−Tph−COF−Dct and the intermediate architectures are summarized in Figure 4d and Figure S31. *COH formation serves as the rate-determining step ($\Delta G = 1.05$ eV) for the four non-spontaneous reaction steps with $\Delta G > 0$, including the formation of *COOH, *COH, $*CH_2OH$ and $*CH_2$.

Above all, we propose a possible electrochemical CO_2-to-CH_4 pathway on Cu−Tph−COF−Dct to better understand the catalysis process. CO_2 is firstly adsorbed and activated on the Dct and Cu center, which are quickly transformed into *COOH. Then, a large amount of CO is formed on Dct to increase the concentration of CO. Subsequently, CO generated on Dct would further transfer to Cu center in the nanosheet morphology to further increase the CO concentration around Cu center. After that, the *COH, *CHOH, $*CH_2OH$, $*CH_2$, $*CH_3$ and $*CH_4$ intermediates generate in turn involves the reduction of CO_2 along with (H^+/e^-) pairs and the desorption of H_2O. Finally, the produced CH_4 is quickly desorbed from the catalyst surface and efficiently transferred into electrolyte to finish the catalysis process.

Conclusion

In summary, we have provided a strategy based on functionalizing exfoliation agent to simultaneously modify and exfoliate COF into large-scale (≈1.0 μm) and ultrathin (≈3.8 nm) nanosheet and explored its electrochemical CO_2RR performance. This strategy enables the lightweight exfoliated-COF to achieve largely enhanced selectivity of CO_2-to-CH_4. Specifically, Cu−Tph−COF−Dct, which comprises sequential Cu-porphyrin and Dct catalysis units, exhibits a superior FE of ≈80% and current density of $-220.0\ mA\,cm^{-2}$ for CH_4 at −0.90 V, which is almost doubly enhanced when compared with bare COF and superior to most of Cu-based electrocatalysts for CO_2RR to CH_4. The FE_{CH4} keeps higher than 68% over a potential range from −0.8 to −1.0 V. Moreover, the vital role of Dct as CO_2 reduction auxiliary and the detailed catalytic mechanism are systematically studied by the DFT calculations. The immobilized functionalizing exfoliation agent (Dct groups) with integrated amino and triazine groups can strengthen the absorption/activation of CO_2, stabilize the active intermediates and facilitate the generation of CO to enrich the CO concentration around Cu active sites, which endow an enhanced catalytic activity towards CH_4 production. The design of COF-based electrocatalysts that enable simultaneous molecular functionalization and exfoliation would be a very effective way to achieve efficient CO_2RR toward valuable products.

Acknowledgements

This work was financially supported by NSFC (No. 22171139, 21871141, 21871142, 22071109 and 21901122); the NSF of Jiangsu Province of China (No. BK20171032); the Natural Science Research of Jiangsu Higher Education Institutions of China (No. 19KJB150011) and Project funded by China Postdoctoral Science Foundation (No. 2019M651873); Priority Academic Program Development of Jiangsu Higher Education Institutions and the Foundation of Jiangsu Collaborative Innovation Center of Biomedical Functional Materials. The Postgraduate Research & Practice Innovation Program of Jiangsu Province (KYCX21 1328).

Conflict of Interest

The authors declare no conflict of interest.

Keywords: CO producing site · Electrocatalytic CO_2 reduction reaction · methane · nanosheet

[1] a) H. Rao, L. C. Schmidt, J. Bonin, M. Robert, *Nature* **2017**, *548*, 74–77; b) J. E. Huang, F. Li, A. Ozden, A. Sedighian Rasouli, F. P. García de Arquer, S. Liu, S. Zhang, M. Luo, X. Wang, Y. Lum, Y. Xu, K. Bertens, R. K. Miao, C.-T. Dinh, D. Sinton, E. H. Sargent, *Science* **2021**, *372*, 1074; c) J. Bednar, M. Obersteiner, A. Baklanov, M. Thomson, F. Wagner, O. Geden, M. Allen, J. W. Hall, *Nature* **2021**, *596*, 377—383.

[2] a) F. P. García de Arquer, C.-T. Dinh, A. Ozden, J. Wicks, C. McCallum, A. R. Kirmani, D.-H. Nam, C. Gabardo, A. Seifitokaldani, X. Wang, Y. C. Li, F. Li, J. Edwards, L. J. Richter, S. J. Thorpe, D. Sinton, E. H. Sargent, *Science* **2020**, *367*, 661 – 666; b) X. Chen, J. Chen, N. M. Alghoraibi, D. A. Henckel, R. Zhang, U. O. Nwabara, K. E. Madsen, P. J. A. Kenis, S. C. Zimmerman, A. A. Gewirth, *Nat. Catal.* **2021**, *4*, 20 – 27; c) Y.-R. Wang, Q. Huang, C.-T. He, Y. Chen, J. Liu, F.-C. Shen, Y.-Q. Lan, *Nat. Commun.* **2018**, *9*, 4466; d) Y. C. Tan, K. B. Lee, H. Song, J. Oh, *Joule* **2020**, *4*, 1104 – 1120; e) Y.-R. Wang, R.-X. Yang, Y. Chen, G.-K. Gao, Y.-J. Wang, S.-L. Li, Y.-Q. Lan, *Sci. Bull.* **2020**, *65*, 1635 – 1642.

[3] a) M. G. Kibria, J. P. Edwards, C. M. Gabardo, C.-T. Dinh, A. Seifitokaldani, D. Sinton, E. H. Sargent, *Adv. Mater.* **2019**, *31*, 1807166; b) O. S. Bushuyev, P. De Luna, C. T. Dinh, L. Tao, G. Saur, J. van de Lagemaat, S. O. Kelley, E. H. Sargent, *Joule* **2018**, *2*, 825 – 832.

[4] a) F. N. Al-Rowaili, A. Jamal, M. S. Ba Shammakh, A. Rana, *ACS Sustainable Chem. Eng.* **2018**, *6*, 15895 – 15914; b) J. Liu, D. Yang, Y. Zhou, G. Zhang, G. Xing, Y. Liu, Y. Ma, O. Terasaki, S. Yang, L. Chen, *Angew. Chem. Int. Ed.* **2021**, *60*, 14473 – 14479; *Angew. Chem.* **2021**, *133*, 14594 – 14600; c) J.-D. Yi, R. Xie, Z.-L. Xie, G.-L. Chai, T.-F. Liu, R.-P. Chen, Y.-B. Huang, R. Cao, *Angew. Chem. Int. Ed.* **2020**, *59*, 23641 – 23648; *Angew. Chem.* **2020**, *132*, 23849 – 23856.

[5] a) Z. Liang, H.-Y. Wang, H. Zheng, W. Zhang, R. Cao, *Chem. Soc. Rev.* **2021**, *50*, 2540 – 2581; b) X. Zhi, A. Vasileff, Y. Zheng, Y. Jiao, S.-Z. Qiao, *Energy Environ. Sci.* **2021**, *14*, 3912 – 3930.

[6] a) H. Xu, D. Rebollar, H. He, L. Chong, Y. Liu, C. Liu, C.-J. Sun, T. Li, J. V. Muntean, R. E. Winans, D.-J. Liu, T. Xu, *Nat. Energy* **2020**, *5*, 623 – 632; b) G. Liu, M. Lee, S. Kwon, G. Zeng, J. Eichhorn, A. K. Buckley, F. D. Toste, W. A. Goddard, F. M. Toma, *Proc. Natl. Acad. Sci. USA* **2021**, *118*, e2012649118.

[7] a) X.-F. Qiu, H.-L. Zhu, J.-R. Huang, P.-Q. Liao, X.-M. Chen, *J. Am. Chem. Soc.* **2021**, *143*, 7242 – 7246; b) H. Zhong, M. Ghorbani-Asl, K. H. Ly, J. Zhang, J. Ge, M. Wang, Z. Liao, D. Makarov, E. Zschech, E. Brunner, I. M. Weidinger, J. Zhang, A. V. Krasheninnikov, S. Kaskel, R. Dong, X. Feng, *Nat. Commun.* **2020**, *11*, 1409.

[8] a) X. Yuan, S. Chen, D. Cheng, L. Li, W. Zhu, D. Zhong, Z.-J. Zhao, J. Li, T. Wang, J. Gong, *Angew. Chem. Int. Ed.* **2021**, *60*, 15344 – 15347; *Angew. Chem.* **2021**, *133*, 15472 – 15475; b) T.-C. Chou, C.-C. Chang, H.-L. Yu, W.-Y. Yu, C.-L. Dong, J.-J. Velasco-Vélez, C.-H. Chuang, L.-C. Chen, J.-F. Lee, J.-M. Chen, H.-L. Wu, *J. Am. Chem. Soc.* **2020**, *142*, 2857 – 2867.

[9] a) S. Popović, M. Smiljanić, P. Jovanovič, J. Vavra, R. Buonsanti, N. Hodnik, *Angew. Chem. Int. Ed.* **2020**, *59*, 14736 – 14746; *Angew. Chem.* **2020**, *132*, 14844 – 14854; b) S. Nitopi, E. Bertheussen, S. B. Scott, X. Liu, A. K. Engstfeld, S. Horch, B. Seger, I. E. L. Stephens, K. Chan, C. Hahn, J. K. Nørskov, T. F. Jaramillo, I. Chorkendorff, *Chem. Rev.* **2019**, *119*, 7610 – 7672.

[10] a) Y. Wang, J. Liu, G. Zheng, *Adv. Mater.* **2021**, 2005798; b) Y. Lum, J. W. Ager, *Energy Environ. Sci.* **2018**, *11*, 2935 – 2944; c) D. Gao, R. M. Arán-Ais, H. S. Jeon, B. Roldan Cuenya, *Nat. Catal.* **2019**, *2*, 198 – 210.

[11] a) X. She, T. Zhang, Z. Li, H. Li, H. Xu, J. Wu, *Cell Rep. Phys. Sci.* **2020**, *1*, 100051; b) H. Zhang, X. Chang, J. G. Chen, W. A. Goddard, B. Xu, M.-J. Cheng, Q. Lu, *Nat. Commun.* **2019**, *10*, 3340; c) A. Khorshidi, J. Violet, J. Hashemi, A. A. Peterson, *Nat. Catal.* **2018**, *1*, 263 – 268.

[12] Y.-J. Zhang, V. Sethuraman, R. Michalsky, A. A. Peterson, *ACS Catal.* **2014**, *4*, 3742 – 3748.

[13] J. Sisler, S. Khan, A. H. Ip, M. W. Schreiber, S. A. Jaffer, E. R. Bobicki, C.-T. Dinh, E. H. Sargent, *ACS Energy Lett.* **2021**, *6*, 997 – 1002.

[14] a) D. Ren, B. S.-H. Ang, B. S. Yeo, *ACS Catal.* **2016**, *6*, 8239 – 8247; b) D. Ren, J. Gao, L. Pan, Z. Wang, J. Luo, S. M. Zakeeruddin, A. Hagfeldt, M. Grätzel, *Angew. Chem. Int. Ed.* **2019**, *58*, 15036 – 15040; *Angew. Chem.* **2019**, *131*, 15178 – 15182.

[15] C. G. Morales-Guio, E. R. Cave, S. A. Nitopi, J. T. Feaster, L. Wang, K. P. Kuhl, A. Jackson, N. C. Johnson, D. N. Abram, T. Hatsukade, C. Hahn, T. F. Jaramillo, *Nat. Catal.* **2018**, *1*, 764 – 771.

[16] a) C. Gropp, T. Ma, N. Hanikel, O. M. Yaghi, *Science* **2020**, *370*, eabd6406; b) X. Han, C. Yuan, B. Hou, L. Liu, H. Li, Y. Liu, Y. Cui, *Chem. Soc. Rev.* **2020**, *49*, 6248 – 6272; c) X. Guan, F. Chen, Q. Fang, S. Qiu, *Chem. Soc. Rev.* **2020**, *49*, 1357 – 1384; d) T. Ma, E. A. Kapustin, S. X. Yin, L. Liang, Z. Zhou, J. Niu, L.-H. Li, Y. Wang, J. Su, J. Li, X. Wang, W. D. Wang, W. Wang, J. Sun, O. M. Yaghi, *Science* **2018**, *361*, 48.

[17] a) R. Liu, K. T. Tan, Y. Gong, Y. Chen, Z. Li, S. Xie, T. He, Z. Lu, H. Yang, D. Jiang, *Chem. Soc. Rev.* **2021**, *50*, 120 – 242; b) Y. Liu, W. Zhou, W. L. Teo, K. Wang, L. Zhang, Y. Zeng, Y. Zhao, *Chem* **2020**, *6*, 3172 – 3202; c) B. Gui, G. Lin, H. Ding, C. Gao, A. Mal, C. Wang, *Acc. Chem. Res.* **2020**, *53*, 2225 – 2234.

[18] H.-J. Zhu, M. Lu, Y.-R. Wang, S.-J. Yao, M. Zhang, Y.-H. Kan, J. Liu, Y. Chen, S.-L. Li, Y.-Q. Lan, *Nat. Commun.* **2020**, *11*, 497.

[19] S. Kandambeth, D. B. Shinde, M. K. Panda, B. Lukose, T. Heine, R. Banerjee, *Angew. Chem. Int. Ed.* **2013**, *52*, 13052 – 13056; *Angew. Chem.* **2013**, *125*, 13290 – 13294.

[20] D. Mullangi, S. Shalini, S. Nandi, B. Choksi, R. Vaidhyanathan, *J. Mater. Chem. A* **2017**, *5*, 8376 – 8384.

[21] Y. Weng, S. Guan, L. Wang, H. Lu, X. Meng, G. I. N. Waterhouse, S. Zhou, *Small* **2020**, *16*, 1905184.

[22] a) D. M. Weekes, D. A. Salvatore, A. Reyes, A. Huang, C. P. Berlinguette, *Acc. Chem. Res.* **2018**, *51*, 910 – 918; b) S. Chen, Y. Su, P. Deng, R. Qi, J. Zhu, J. Chen, Z. Wang, L. Zhou, X. Guo, B. Y. Xia, *ACS Catal.* **2020**, *10*, 4640 – 4646; c) C. M. Gabardo, C. P. O'Brien, J. P. Edwards, C. McCallum, Y. Xu, C.-T. Dinh, J. Li, E. H. Sargent, D. Sinton, *Joule* **2019**, *3*, 2777 – 2791.

[23] G. L. De Gregorio, T. Burdyny, A. Loiudice, P. Iyengar, W. A. Smith, R. Buonsanti, *ACS Catal.* **2020**, *10*, 4854 – 4862.

[24] Z. Weng, Y. Wu, M. Wang, J. Jiang, K. Yang, S. Huo, X.-F. Wang, Q. Ma, G. W. Brudvig, V. S. Batista, Y. Liang, Z. Feng, H. Wang, *Nat. Commun.* **2018**, *9*, 415.

[25] a) N. J. Firet, W. A. Smith, *ACS Catal.* **2017**, *7*, 606 – 612; b) Y. Katayama, F. Nattino, L. Giordano, J. Hwang, R. R. Rao, O. Andreussi, N. Marzari, Y. Shao-Horn, *J. Phys. Chem. C* **2019**, *123*, 5951 – 5963; c) X. Li, Y. Sun, J. Xu, Y. Shao, J. Wu, X. Xu, Y. Pan, H. Ju, J. Zhu, Y. Xie, *Nat. Energy* **2019**, *4*, 690 – 699; d) E. Pérez-Gallent, M. C. Figueiredo, F. Calle-Vallejo, M. T. M. Koper, *Angew. Chem. Int. Ed.* **2017**, *56*, 3621 – 3624; *Angew. Chem.* **2017**, *129*, 3675 – 3678; e) S. Zhu, T. Li, W.-B. Cai, M. Shao, *ACS Energy Lett.* **2019**, *4*, 682 – 689.

Manuscript received: October 28, 2021
Accepted manuscript online: November 21, 2021
Version of record online: December 18, 2021